Spatially Resolving the Magnetic Configuration of Trilayer Submicrometer Disks with Vortex Chiral Asymmetry Using X-Ray Resonant Magnetic Scattering

J. Díaz [1,2,*] L.M. Álvarez-Prado [1,2] S.M. Valvidares,[3] I. Montoya,[4] C. Redondo [4] R. Morales [5,6] and M. Vélez [1,2]

[1] *Universidad de Oviedo, Calle Federico García Lorca 18, Oviedo 33007, USA*
[2] *CINN (CSIC—Universidad de Oviedo), El Entrego 33940, Spain*
[3] *ALBA Synchrotron, Cerdanyola del Vallés 08290, Spain*
[4] *Department of Physical Chemistry, University of the Basque Country UPV/EHU, Leioa E-48940, Spain*
[5] *Department of Physical Chemistry, University of the Basque Country UPV/EHU and BCMaterials, Leioa E-48940, Spain*
[6] *IKERBASQUE, Basque Foundation for Science, Bilbao E-48011, Spain*

We show that, in the x-ray magnetic resonant scattering (XRMS) of a two-dimensional array of submicron magnets, the collected intensity at each Bragg reflection is correlated to the reflected light from locations of the magnets that have the same angle of curvature. This converts XRMS in a kind of magnetic microscope capable of spatially resolving the magnetization of the small-size magnets, averaged over the magnets illuminated by the x rays. This result is used to study the magnetization of trilayer submicron disk-shaped magnets consisting of two magnetostatically coupled ferromagnetic layers, about 15 nm thick, separated by a nonmagnetic spacer. These kinds of systems are less known than the single-layer ones, despite having potentially more interesting functionalities for device applications, mainly due to the difficulty to distinguish the magnetization of each of the layers within the magnets. This problem is overcome by XRMS thanks to its chemical sensitivity and its relatively large depth probe. XRMS is also a photon-in photon-out technique that allows measuring under external magnetic fields. This permits the extraction of the local hysteresis loops at different locations of the disks. The technique demonstrates to be very sensitive to the magnetization distribution across each of the layers at any field intensity, with an estimated lateral resolution below 200 nm. This serves to detect, and also explain, chiral asymmetries in the magnetic circulation of the vortex in each of the layers.

I. INTRODUCTION

Magnetic vortices formed in single magnets have been the subject of investigation since the methods to create arrays of submicron size magnets have been available [1–5]. They are a stable magnetic configuration in disks and square magnets, and they are relatively simple to describe. An interesting aspect of the vortex is that it can adopt four different configurations, attending to the handiness of the magnetic rotation and the sense of polarization of its core. These configurations are robust and they have been intended to be used for information storage [6,7], as a spin-wave source [8,9], as magnetic sensors [10–12], and in biotechnology [13,14]. The difference in energy between the configurations depends on the symmetries of the system in many cases, and its characterization and control has been a subject of investigation for years.

The behavior of stacking magnetic layers in the same shaped magnet is, however, less known. A double-layer system allows more parameters to tune, for instance, the interaction between layers through the nonmagnetic spacer and the magnetization of the disks, increasing its functional capabilities [11,15]. Such a double-layer structure is actually chosen in sensors and memory units, such as in spin valves and magnetic tunnel junctions. However, the studies using magnets with more than one magnetic layer are scarce due to the more difficult characterization of the buried layers [8,16,17]. Most of the magnetic sensitive microscopies with submicron resolution are surface sensitive, such as magnetic force microscopy (MFM) [18–21] and photoemission electron microscopy (PEEM) [22]. Transmission electron microscopies are not layer sensitive [2,15,23]. They are also subjected to limitations in the type of substrates, which have to be transparent to electrons, and in the range of applied fields during measurements.

*jidiaz@uniovi.es

These limitations are overcome in x-ray magnetic resonant scattering (XRMS), making it the tool of choice for the characterization of these systems due to its capability to peer into buried layers at relatively large thickness. XRMS is a nondestructive photon-in photon-out technique, which makes it compatible with the use of external fields, currents, or temperature during measurements. The only restriction for the sample substrates is to be flat. The principles of magnetic scattering are similar to those observed using light in the visible spectrum [24–28]. Changing the polarization of the incident beam allows either measurement of the longitudinal or the transverse component of the magnetization of the probed magnets [27,29]. Using x rays permits access to a wider range of moment-transfer values, increasing the sensitivity to local changes. To distinguish the magnetic signal from each of the stacking layers, the energy and polarization of the x rays must be tuned, requiring a synchrotron radiation source.

XRMS has been already used in this kind of system before [16,30,31]. In particular, the study performed in Ref. [32] is the only one that recovers the magnetization of each layer in a bilayer square-ring magnet at different subregions by deconvoluting the contribution of each of these subregions to the intensity of the diffracted spots. This method requires magnets with geometrically well-differentiated regions and form factors. In all the cases, it is assumed that the magnets are flat, i.e., perfectly bidimensional. However, this is not always the case [33]. Short wavelength sources can be specially sensitive to this. The present study deepens the interpretation of the intensity obtained at different x-ray Bragg-reflected angles for those cases in which the form of the magnets is not perfectly flat, finding a correlation between the angle at which the Bragg reflection (BR) is collected and the region of the submicron magnet from where the light comes. For those cases, this converts XRMS in a magnetic microscope capable of seeing the variations in the lateral component of the magnetization, averaged over all the submicron magnets illuminated by the x rays, at specific regions of the submicron magnets and at specific layers. It also evidenced the sensitivity of XRMS to the morphology of the disks in a quantitative way, making it possible to determine changes in the thickness across the area of the submicron magnets with nanometer resolution. This is an aspect that has been largely overlooked, since most of the studies carried out assumed that the shape of the magnets was perfectly flat.

A direct consequence of this finding has to do with the sensitivity of the XRMS to the chiral asymmetry of the vortex. This sensitivity was demonstrated by us in a previous experiment on an array of a single layer of Permalloy disks [34]. This sensitivity arises in XRMS from the origin of the magnetic scattering intensity in these systems, which is due to the interference between the magnetic and charge scattering, and it has a similar origin as that observed using visible light [27,28]. Although this interpretation is still valid in perfectly flat magnets, the present experiment shows that chiral sensitivity is enhanced by the curved surface of the submicron magnets and, probably, by the imperfections in their shape like the roughness of their interfaces.

In the studied sample, chiral asymmetry is detected when the disks' array is oriented at an oblique angle with respect to its easy axis, changing its vortex chiral sense with the direction of the initial magnetization in saturation. Thanks to the here reported microscopic sensitivity of XRMS, the region of the disks where the inversion of the magnetization starts is determined. This serves to demonstrate that the magnetic chiral asymmetry of the disks is associated to a noncentrosymmetric distribution of their magnetization. Chiral symmetry is also detected in each of the layers, resulting in being the same in both. This is in contrast to what is expected if only the magnetostatic coupling between the layers is taken into account, indicating that both layers are affected by the same noncentrosymmetric interaction, and also by an attractive interlayer interaction.

II. SAMPLE PREPARATION AND CHARACTERIZATION

The array of magnets is produced by, first, creating an antidot array by interference laser lithography (ILL) on a negative resist that is spin wet on silicon substrates. The ILL procedure uses Lloyd's mirror interferometer with a He-Cd laser ($\lambda = 325$ nm) as the light source [35]. ILL produces patterns of a constant period and similar magnet shape over large areas of the order of cm^2 in a single shot. In this way, the x-ray beam has no restrictions in its size to probe the samples. The metallic layers are deposited on these antidot-imprinted substrates by magnetron sputtering. The measured submicron magnet array results after the resist is lifted off. Evaporation of each layer is done at normal incidence in a vacuum chamber at a base pressure of 1×10^{-7} mbar and under an Ar pressure of 3×10^{-3} mbar. The iron layer is 14.8 nm thick, and it is deposited directly on the substrate with no buffer layer, following by the deposited of the aluminum spacer layer (2.2 nm) and the cobalt layer (17.6 nm). A 3-nm aluminum capping layer is deposited on top to avoid contamination.

A reference sample is deposited at the same time as the substrates with the imprinted pattern. Figure 1 shows the hysteresis loops of the reference and the patterned samples measured by VSM. The reference sample is magnetically soft, with an in-plane magnetic anisotropy of about 4 mT and a coercive field in the easy axis (EA) of about 1.5 mT. The hysteresis loops of the magnets' array are what is expected in magnetic configurations that minimize their stray magnetic fields, with low remanence, coercivity, and
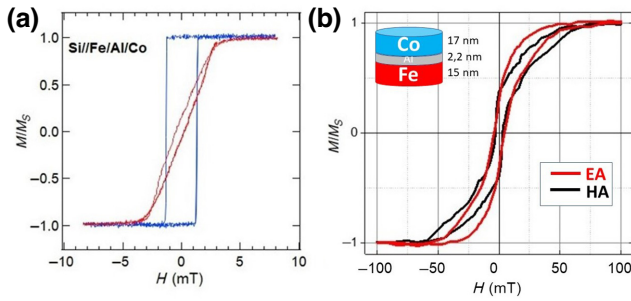
FIG. 1.   (a) Hysteresis loops of a reference thin film prepared at the same time as the array of disks; (b) VSM hysteresis loops of the two-dimensional array of disks along the EA (red line), parallel to the (01), and to the HA , parallel to the (10) direction of the square lattice.
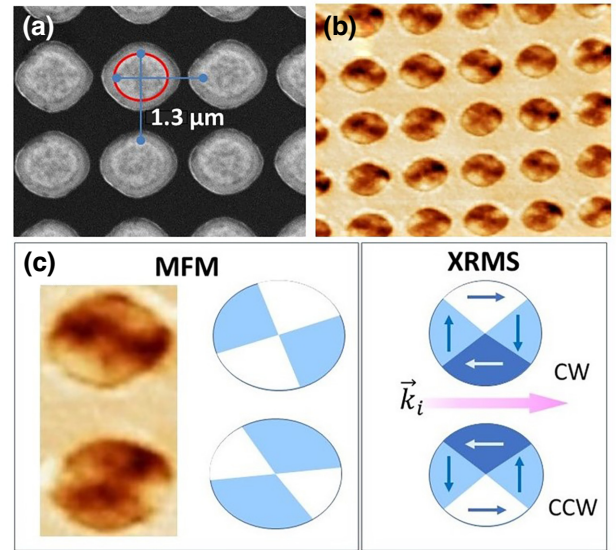

FIG. 2.   (a) SEM image of the array of disks; (b) MFM image of the array of disks; (c) detail of the MFM image of two disks with vortices formed with opposite magnetic circulation directions. MFM can distinguish between the two chiral states in a vortex but it cannot tell its rotation direction. The same panel compares it with what is observed by XRMS: in the grazing angle geometry using circularly polarized light, XRMS is sensitive to the magnetic components parallel (white region) or antiparallel (dark blue region) to the incident beam (light purple arrow), unveiling the rotation direction of the vortex formed in the disk. At grazing incidence, XRMS is not sensitive to the polar orientation of the core (not shown in the figure).

comparatively large saturation fields. Its relative remanence M_r/M is of the order of 30%, and its coercive field is of about 2 mT. The saturation field of the sample changes from 55 mT to more than 70 mT at two orthogonal directions parallel to the symmetry axis of the square lattice of the array. These values are of the same order or even larger than that observed in single-layer disks of similar diameter (800 nm) in arrays where the intermagnet interaction is negligible [36]. This is likely due to the magnetostatic interlayer interaction, which increases the energy required to saturate the disks. The observed smaller saturation field in the EA might be due to the small ellipsoidal shape of the disks, and, possibly, to the difference in the intermagnet interaction due to the consequent difference in the distance between magnets.

SEM images show that the lattice is perfectly squared with a lattice parameter, α, of 1.3 µm, confirmed by the x-ray diffracted pattern. The magnets have a diamond shape with rounded corners approaching the shape of a disk. The corners are aligned to the square-lattice axis. The axis of the magnet related to these directions of the array do not have the same length: their proportion ratio is of about 0.9 [see Fig. 2(a)]. The size of the disks is 805 nm in the long axis. The EA of the sample is parallel to this axis. MFM images confirm the presence of a single vortex at the top layer of most of the disks in the remanent state of the samples [see Fig. 2(b)]. It is worthwhile to highlight here that, although MFM can detect indirectly a magnetic circulation in the vortex and the presence of chiral asymmetries, it cannot determine by itself its circulation sense [18,19]. Figure 2(c) shows the difference between MFM, which is sensitive to the perpendicular component of the stray field produced by the disk, and XRMS, which is sensitive to the component of the magnetization parallel to the direction of the incident beam when circularly polarized light is used.

The x-ray scattering experiment is done at the MARES endstation of the BOREAS beamline, in the ALBA synchrotron [37]. In this beamline, 100% circular polarization

is generated by an undulator. Figure 3 shows the geometry and the axis orientation for the q_x, q_y components of the moment transfer vector $\vec{q}$ used in the CCD images. $\vec{q} = \vec{k}_{sct} - \vec{k}_i$, being $\vec{k}_i$ and $\vec{k}_{sct}$ the wave vectors of the incident and the scattered beams, respectively. For the reflectivity measurements, the CCD camera is substituted by a x-ray detector.

The thickness of the deposited layer and the quality of their interfaces is obtained by fitting the resonant reflectivity curves of the reference sample taken at the Fe and Co resonant energies using circularly polarized light. Figure 4 displays the reflectivity curves and the magnetic dichroism asymmetry with their corresponding fitting curves obtained at the L_3 resonant energies of Fe (706 eV) and Co (777 eV). The fitting of the curves is done by a homemade code using the methodology presented in Ref. [38]. The thickness of the cobalt and iron layers are 176 and 148 Å respectively. Their thickness ratio is chosen to be approximately the same as their magnetization ratio, which is 0.84, to have the same magnetization in the two layers. The thickness of the aluminum spacer is about 22 Å, which is large enough to consider that the magnetic interaction between layers is entirely dipolar. The interfaces of the cobalt and Fe layers with the nonmagnetic aluminum
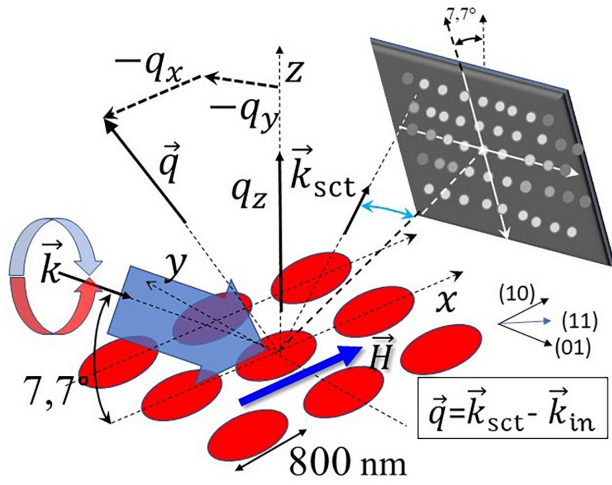
FIG. 3. Geometry of the scattering experiment: orientation of the q_x and q_y axis with respect to the incident, $\vec{k}_i$, and scattered, $\vec{k}_{sct}$, beams.

spacer have a roughness of about 9 Å. This value might include some possible intermixing between layers.

Resonant magnetic reflectivity curves are also obtained from the disks, which are displayed in Fig. 5. Oscillations due to magnetic contrast are visible and they are used to determine the x-ray incident angle under which magnetic contrast is the highest in the range of large q_x values. However, the curves cannot be fitted in the same way as the reference sample, likely due to the discrete nature of the probed surface, which might introduce intensity unrelated to pure reflection from the disks.

III. MAGNETIC SCATTERING

The scattering of x rays is sensitive to the magnetic moment of the probed material by considering the terms of the photon scattering that are sensitive to the angular moment of the electrons. These terms are usually too small
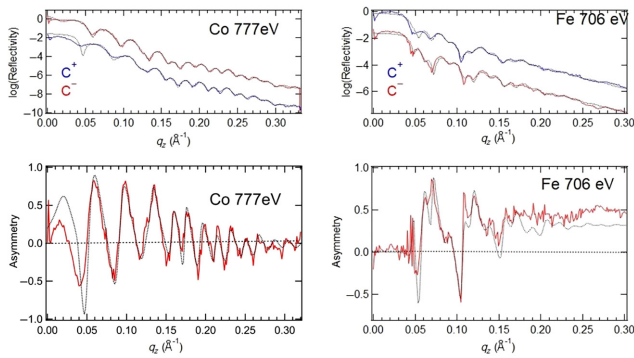

FIG. 4. Fitted reflectivity and magnetic asymmetry curves of the reference thin film taken at the (a) Co (776 eV) and (b) Fe (706 eV) edges .
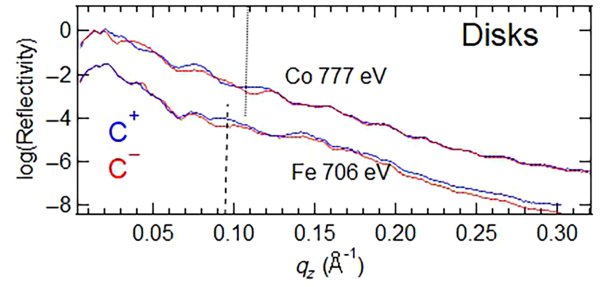

FIG. 5. Reflectivity curves of the array of disks taken at the cobalt (776 eV) and iron (706 eV) edges. The position in $q_z(\theta_i)$ chosen for obtaining the diffraction patterns with magnetic contrast are marked in each curve with a vertical line.

but they are enhanced when the photon energy is close to the absorption edge of the probed element where its magnetic properties are better manifested, the scattering becoming element specific. In this case, the chosen photon energies are 706 and 777 eV, the energies of the L_3 edge for Fe and Co, respectively. Using circular polarized light and grazing incidence, the intensity observed is, to a good approximation, proportional to the scalar product between the scattered magnetic moment of the electron, $\vec{m}_{3d}$, and the wave vector of the incident beam, $\vec{k}_i$. In the present experiment, magnetic contrast is obtained at the BR directions only, indicating that this king of scattering corresponds to the term related to the interference between the charge scattering and the magnetic scattering. This scattered intensity, I_{MQi}, has the following dependence on the scattering vectors and the magnetic configuration of the disks [29]:

$$
\begin{aligned}
I_{MQi} &= \mathrm{Re}\left[F_0^* \rho^*(\vec{q}) F_1 \left(\vec{k}_i \cdot \mathbf{M}(\vec{q}) \right.\right. \\
&\quad \left.\left. + \vec{k}_{sct} \cdot \mathbf{M}(\vec{q}) \left(\vec{k}_i \cdot \vec{k}_{sct} \right) \right) \right] P_3 \\
&\approx 2\mathrm{Re}\left[F_0^* \rho^*(\vec{q}) F_1 \vec{k}_i \cdot \mathbf{M}(\vec{q}) \right] P_3.
\end{aligned}
\tag{1}
$$

$\mathbf{M}(\vec{q})$ and $\rho^*(\vec{q})$ are the Fourier transform of the magnetic and charge configuration of the array of disks, F_0 and F_1 are the scattering factors for charge and magnetic scattering, P_3 is the circular polarization degree and $\vec{q} = \vec{k}_{sct} - \vec{k}_i$ is the moment transfer vector.

The structure and magnetic characterization of the samples is done measuring the reflectivity curves over a relatively wide range of 2θ angles, from $0°$ to $50°$ using a photodiode detector. The light scattered from the two-dimensional array is detected using a CCD camera placed at the same location as the photodiode. Magnetic fields are set at constant values for each measurement using a dedicated electromagnet [39]. Magnetic contrast at the BRs in the CCD images at each magnetic field intensity is obtained by calculating the circular dichroism:

$I_M(\vec{q}) = I_{MQi}^{C^+} - I_{MQi}^{C^-}$. Charge scattering is extracted summing the intensity obtained at the two circular polarization helicities, $I_M(\vec{q}) = I_{MQi}^{C^+} + I_{MQi}^{C^-}$.

The photon energy and incidence angle chosen are those in which the dichroism contrast occurred at a similar angle for the Co and Fe edges to ensure that the probed areas of the sample are nearly the same. The chosen angle of incidence is $\theta_i = 7.7°$, which is high enough to include a large number of BRs in the q_x direction, parallel to the direction of the beam.

Figure 5 indicates, in the q_z scale ($q_z = 2k_0 \sin\theta_i, k_0 = 2\pi/\lambda$), the dichroism contrast for that angle of incidence at the iron and cobalt chosen photon energies. A total of ten snapshots with 0.1' exposure are recorded to obtain the final Bragg intensity pattern covered by the CCD camera at each of the applied magnetic fields for each circular polarization helicity, C^+ and C^-, of the incident x rays. This process is repeated at different applied fields to complete the two branches of an hysteresis loop (HL). Each of the branches consisted of 30 measurements at constant increments of the applied magnetic field, where $\Delta H = 4.7$ mT. HL started measuring at magnetic saturation fields of 70 mT. The measurements are done in two different orientations of the disks' arrays with respect to the magnetic field: (1) at the (11) orientation of the array, oblique to its magnetic easy axis (EA), and (2) at the (10) orientation, parallel to the EA.

IV. BRAGG REFLECTIONS

Figure 6 displays the diffraction patterns recorded on the CCD at the Co and Fe resonant energies, 776 and 706 eV, respectively, in the (11) array orientations. Their corresponding profiles along the q_y direction for all the q_x values collected are depicted in Fig. 7. The figures contain the diffraction pattern due to the scattering of the charge ($I_Q(\vec{q})$) and the magnetic dichroism ($I_M(\vec{q})$) obtained with the sample in magnetic saturation. The images are scaled in the q_x and q_y components of the moment transfer. Due to the grazing incidence geometry, the range of q_x values collected by the CCD camera is smaller than in the q_y direction. The dynamic range in the CCD images are reduced to enhance the intensity of Bragg reflections at angles far from the reflected beam, which is the most intense.

The intensity of the diffraction pattern spreads from the center of the image, with more intensity at positive than at negative q_x values. This intensity is also modulated, i.e., its value oscillates from the center of the pattern, apparently forming parabolic curves with their vertex located at the positive side of the q_x axis. Both (10) and (11) orientations have a similar intensity distribution pattern. There exists marked differences between the distributed intensity in Co and Fe: the intensity at the center looks broader in cobalt than in iron when moving to negative q_x values. In
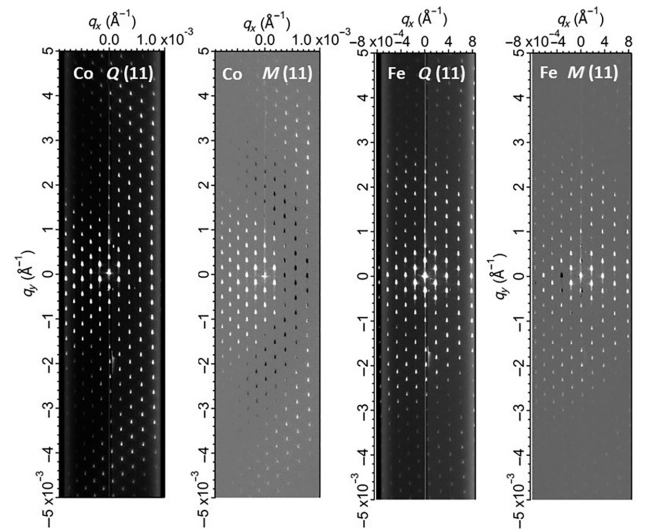

FIG. 6. Diffraction pattern of the two-dimensional array of disks taken at the Co (776 eV) and Fe (706 eV) edges at the (11) orientations due to charge scattering (Q) and magnetic scattering (M). The sample is magnetically saturated during image acquisition.

Fe, the BRs with the lowest intensity near the center of the diffraction pattern forms an incomplete ring. Cobalt magnetic contrast changes sign twice counting from the center to the border. Fe changes the sign of its magnetic contrast in few points just at the center of the image, but there is no change in the sign of the contrast at higher q_y values as in cobalt.

The observed modulation in intensity of the BR peaks cannot be attributed to the diffraction form factor of the disks. Actually, such a diffraction is missing from the pattern. If it existed, it should form concentric circular rings from the center of the pattern since its form factor depends only on the in-plane coordinates x and y, i.e., it is only a function of q_x and q_y. The regular spacing between the BR peaks, which depends on q_x and q_y only, avoids any possible deformation of these rings due to a sample misalignment. The size of the observed rings does not correspond to what is expected from the diameter of the disk. And the intensity outside the first zero in intensity is far higher than that expected from the diffraction of a disk, as deduced from Figs. 6 and 7. For instance, the intensity of the BRs at $q_x = 4q_0$ ($q_0 = 2\pi/\alpha$, and α is the lattice parameter of the array) is comparable to the intensity near the region close to the reflected beam, BR [0, 0].

The described intensity distribution in the diffracted patterns is better explained by assuming that the surface of the disks has a curvature due to a radial decrease in their thickness. In this situation, the x rays are not uniformly reflected across the surface of the disk since the angle of incidence varies from point to point depending on its curvature angle γ. This angle is defined as that formed
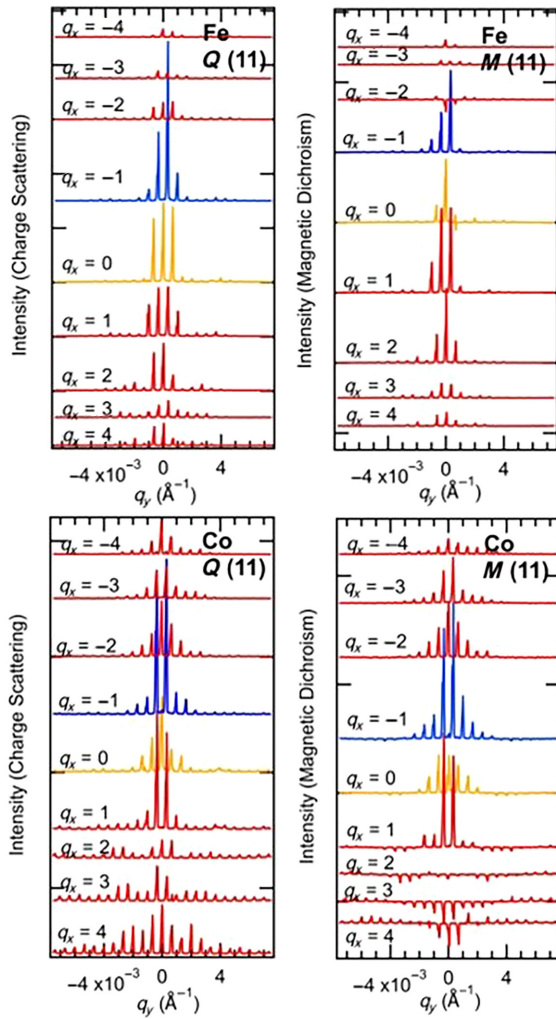
FIG. 7. Charge (*Q*) and magnetic dichroism (*M*) scans along the q_y direction for different values of q_x in iron and cobalt in the (11) orientation. Profiles in $q_x = 0$ and $q_x = -1$ are depicted in different colors to distinguish them from the adjacent profiles.

FIG. 8. Model for the reflection of the x rays from a dome shaped disk. (a) Definition of γ and φ angles; (b) Transverse cut of the model proposed for the structure of the disks. H is the the thickness of the layer at the center of the disks, and τ is the thickness at a distance from the center. γ is the angle formed by the normal to the surface at that point with respect to the z axis; (c),(d), dependence of q_x, q_x and q_x with the angles γ in the longitudinal (*x* axis) and transverse (*y* axis) to the beam directions.

between the normal to the surface at the specific location in the disk, and the normal to the substrate. The steepness of the surface depends on the rate at which the thickness of the layer decreases. The parameter τ defines the thickness of the disk layer at the specific location in the disk. The correlation between τ and γ depends on the morphology of the disk. Figure 8 shows the angles and parameters that describe the proposed three-dimensional shape of the disks.

In this model, the oscillations in intensity are due to the interference between the light scattered at each interface of the multilayered magnet. Therefore, in the case of a single layer, the scattered light with the lowest intensity have the relation $q_z\tau = 2\pi\,(m + 1/2)$, where m is an integer number. Both q_z and τ are correlated to γ, i.e., they depend on the location of the disk from where the light is reflected. The other components of the moment-transfer vector, q_x

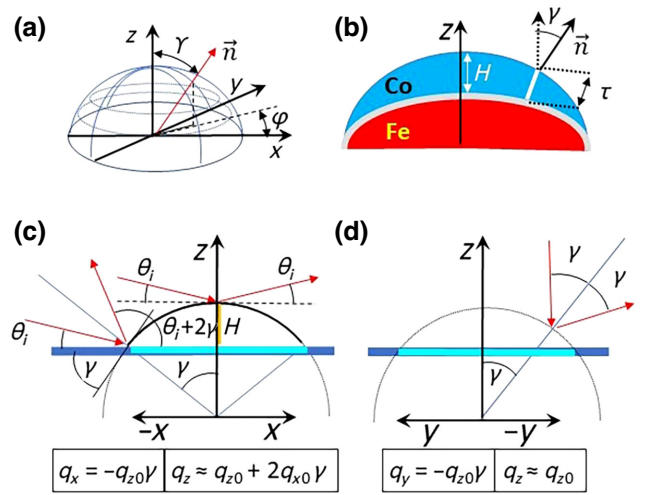and q_y also depends on the orientation and curvature of each point in the disk. Their variation with the angle γ is obtained by defining the plane of incidence at each point in the disk. Taking only the linear terms,

$$q_x \approx q_{z0}\gamma \cos\varphi, \tag{2}$$

$$q_y \approx q_{z0}\gamma \sin\varphi, \tag{3}$$

$$q_z \approx q_{z0} - \frac{q_x}{\theta_i}, \tag{4}$$

$q_{z0} = 2\left|\vec{k}_i\right|\sin\theta_i$. The angle φ is formed by the position of the point in the plane of the disk with respect to the x axis (see Fig. 8). These equalities show that γ is related to the plane component of the moment transfer vector, $q_\parallel$, by the dependence $\gamma = q_\parallel/q_{z0}$. Note that when $q_x = 0$, $q_z = q_{z0}$ and, therefore, the variation along q_y depends only on the variation of the thickness τ. Also, when $q_x > 0$ ($\cos\varphi > 1$), q_z decreases, and increases when $q_x > 0$. This means that the equality $q_z\tau = 2\pi\,(m + 1/2)$ is reached at a lower value of γ (q_x) than the corresponding one in $[0, q_y]$ in the former case, but is further away in $q_x < 0$. Moreover, due to the higher reflectivity coefficients at grazing angles, it is expected that the scattered intensity decreases as the take-off angle of the scattered beam increases, which occurs at $q_x < 0$ (see Fig. 3). All of this agrees with what is experimentally observed (Figs. 6 and 7).

Thanks to this result, it is possible to have access to the morphology of the disks in a more quantitative way. Figure
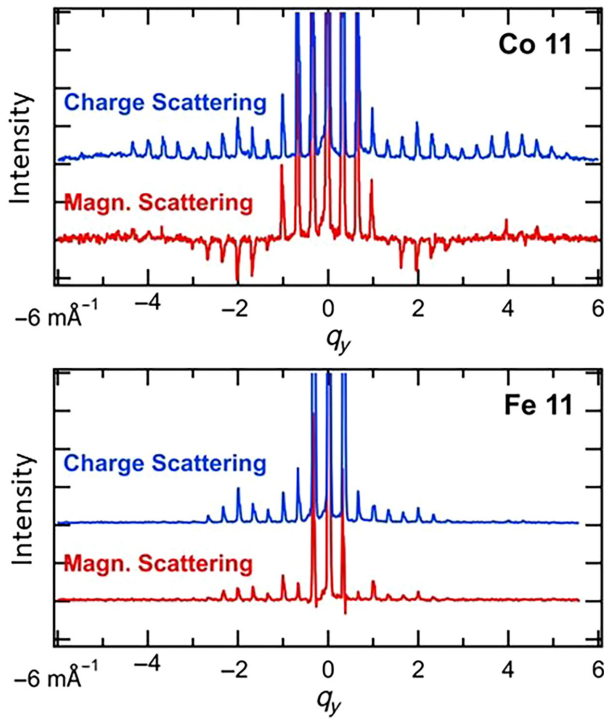
FIG. 9. Intensity profile along the q_y direction at $q_x = 0$ related to the charge scattering (blue) and the magnetic scattering (red) in cobalt (top) and iron (bottom). The profiles are taken with the beam oriented along the (11) direction of the array.

9 shows the $[q_x = 0, q_y]$ profiles of the magnetic dichroism and the charge-scattering intensities measured in cobalt and iron, in the (11) orientation. This profile allows a better estimation of the change of the thickness of the layers across the disks since the change in q_z is practically negligible, all the variations observed are due to the thickness and the steepness of the disk surface. Also, the number of points available are much larger than in the q_x direction. In cobalt, the magnetic contrast is perfectly coupled to the charge scattering: the magnetic contrast changes sign every time the charge scattering has a node. This is what expected in the reflection from a single layer, but not from a trilayer system. Actually, the variation in intensity seems to follow a $\sin^2(q_y)$ function. This suggest that the observed scattered intensity is mainly caused by diffuse scattering at the interfaces of cobalt [40]. This is probably the case since the resonant condition, the large incident angle used ($\theta_i = 7.7°$, which gives rise to a low reflectivity coefficient), and the relatively large roughness of the interfaces.

The profiles of iron have a similar oscillation period than that found in cobalt, but there is one oscillation less. In this case, its magnetic contrast does not change as in cobalt. In fact, it is more structured in the region of highest intensity, in the central region. There, magnetic contrast changes, but it remains constant in the rest of oscillations. This indicates

that the exact understanding of the light scattered from the iron layer is apparently more complicated than in cobalt due to its buried condition. But this complication affects to the magnetic contrast mainly. The oscillation in intensity of the charge scattering is compatible with a single-layer model, as in cobalt, which is the most expected behavior at the resonant photon energy.

Then, the highest order of interference occurs at the point of highest intensity, where the angle $\gamma = 0$ and the thickness is the highest. This is $m = 3$ for cobalt and $m = 2$ for iron due to the lower thickness of the iron layer and the higher wavelength at the iron edge. This agrees with the one less intensity oscillation in iron than in cobalt and the different distribution of the intensity oscillation in the diffraction pattern at both absorption edges shown in Fig. 6. Also, this confirms that the profile along $[0, q_y]$ covers scattered light from all areas of the disk, from the highest thickness to the null thickness regions.

The dependence of the thickness τ on q_y (which is linear on γ) is correlated to the rate at which the thickness of the layer changes with the curvature of the surface, which is unknown. For instance, τ will have a quadratic dependence on q_y if the radius of curvature of the surface of the two interfaces is constant. In that case, the zeros in intensity should occur at q_y values proportional to the square root of the interference order m. However, the experimentally observed relation is close to linear on m (see Fig. 9). This implies that the curvature of the surface of the disks needs to be stronger to have a change in the thickness of the layers. The adjustment of the zeros in the profiles of Fig. 9 is done using the equality $q_z \tau = 2\pi (m + 1/2)$ and taking the relation $\tau = H - (\sigma/2)\gamma = H - \sigma(q_y/2q_{z0})$, where H is the highest thickness of the disk, and σ a factor that indicates how fast the layer thickness changes with the curvature angle. This shows a slightly faster rate in iron than in cobalt, indicating a larger curvature in cobalt than in iron. This relation is expected since cobalt is deposited on a curved surface, whereas iron is deposited in a flat surface. As a consequence of this, there is not a perfect one-to-one correspondence in the intensity of the BRs between cobalt and iron. Iron covers a larger area of the disk in a smaller range of $q_\parallel$ than cobalt. This difference is not excessively relevant. From the previous adjustment of the $[q_x = 0, q_y]$ profile, it is estimated that the curvature of cobalt is of 1.4 times that of iron.

The correlation between a point $[x, y]$ in the disk and the in-plane component of the moment-transfer vector, $\vec{q}_\parallel$, will be distorted if the curvature of the surface is not uniform, i.e., if the variation of the γ angle with the disk position $[x, y]$ is not perfectly linear. This will give rise to a nonuniform distribution of the intensity besides that caused by the thickness. For instance, if the portion of the area of the disk that is flat is large, most of the intensity will be concentrated in a smaller $[q_x, q_y]$ area. On the other hand, thanks to these variations in γ the exact three-dimensional

shape of the magnet could be determined by modeling the resulted changes in the scattered intensity. Note also that the area of the disk covered by the CCD detector is constrained in the q_x direction, related to the x direction. This region is delimited by the first interferential zero due to the gradation in thickness of the disk. Then, the total decrease in thickness covered in the x direction is of the order of 60 Å out of 350 Å, indicating that only the central region of the disk is observed in that direction.

V. HYSTERESIS LOOPS

The one-to-one correlation between the in-plane moment transfer vector and the in-plane spatial coordinate of the disks eases the interpretation of the HLs collected at each BR. For instance, this explains why XRMS is specially sensitive to a chiral asymmetry in the disks: when the vortex is formed, the normal to the surface of the regions of the disks with magnetization parallel to the beam have a component transverse to the field. Therefore, the scattering from these regions has a q_y component. When there is chiral asymmetry in the magnetic vortex circulation, this component points in opposite directions for opposite magnetic orientations, giving rise to the resulting asymmetric magnetic contrast in the q_y axis. This explanation is different, but not contradictory, to the origin of the sensitivity of XRMS to chiral asymmetry proposed in Ref. [34], which still holds and it should be observed in perfect flat disks.

In what follows, it is assumed that each BR position $[h, k]$ is related to a region around a position $[x, y]$ in the disk. To describe the different regions of the disk, the direction of the incident beam is taken as the reference. This direction is the same as the positive direction of the applied field. Therefore, intensity at $q_x > 0$ corresponds to the north (N) side of the disk, $q_x < 0$ to the south (S) side, $q_y > 0$ to the west (W) side and $q_y < 0$ to the east (E) side.

The HLs presented here are normalized to 1. To improve their visualization, their noise is reduced using a binomial smoothing. The smoothing degree is the same for all the loops. This does not modify in essence the loops lineshape since the changes in magnetization should be smooth. However, the smoothing is unable to smearing out all the noise, leaving low-frequency oscillations in the magnetization, which are obviously more notorious in those loops with poorer signal-to-noise ratios. Although this did not impede identifying the general trends, it decreased the accuracy of the onset fields whose highest accuracy is half the field step used to measure the HL, which is 2.3 mT.

Note that the HLs are averaged over hundred of disks. Therefore, the observed result will depend on the possible number of magnetic configurations that the vortex can adopt. This number obviously decreases when the symmetry of the system decreases and the similitude between magnets is increased.

Figure 10 displays the HLs observed at the W (HL$_W$) and E (HL$_E$) sides of the disk, and located relatively distant from the center, when the applied field is oriented parallel to the (11) orientation of the array. The differences between the two HLs are due to the broken chiral symmetry of the magnetic vortex circulation in this orientation. The HLs show changes in the magnetic susceptibility at some critical fields, which define the onset for the creation, movement, and annihilation of the vortex in the disks. The
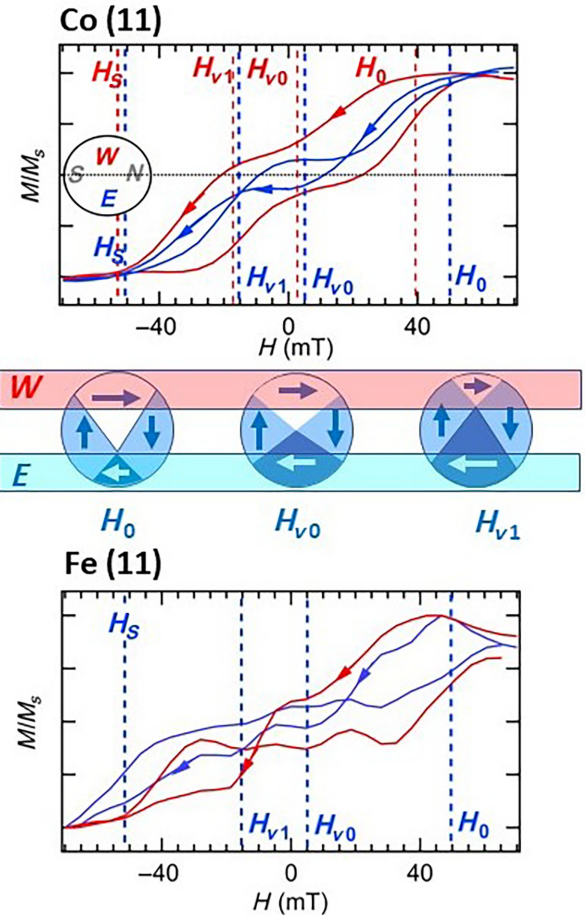

FIG. 10. On top, HLs collected at BRs at fixed q_x but opposite q_y in cobalt at the (11) orientation: in red, $q_y > 0$; and in blue, $q_y < 0$. In the middle, a schematics of the related regions of the disks probed at the corresponding BR orientations: $q_y > 0$ is related to the W side of the disk, and $q_y < 0$ to the E side of the disk. The probed regions are the overlaps between the disks and the related stripes, in the corresponding magnetic configuration of the magnetization of the disks at the fields H_0, H_{v0}, and H_{v1}. The differences between the HLs are due to a fixed magnetic vortex circulation, which is inverted in each branch. In the drawing, N is on the right, S is on the left, W is on the top, and E is on the bottom of the disk. The beam direction goes from S to the N direction. On the bottom, the hysteresis loops taken in iron in the (11) orientation and in similar regions as in cobalt. The values of H_0, H_{v0}, and H_S signaled in the figure of the iron HL are those of the HL$_E$ of cobalt.

field at which the demagnetization of the disk is initiated is named H_0. The location of the disk where this happens is of interest since it sets the circulation sense of the vortex. Note that this means that, if the two branches of the loop are symmetrical, the nucleation occurs always in the same side making the sense of circulation in the vortex to invert in each branch. In the presented example, nucleation occurs in the E side, where H_0 is the highest, about 50 mT. Therefore, the circulation is clockwise (CW) in the downward branch and counter clockwise (CCW) in the upward branch. The creation of the vortex causes a fast reduction of the magnetization until a point where the magnetization reaches a value close to zero and the magnetic susceptibility changes again. The field where this occurs is named H_{v0}. In this case, $H_{v0} = 5$ mT, and it is the same for the E and W side HLs. Once the vortex is formed, the region of the disk with opposite magnetization to the initial one is mainly located in the E side if the circulation is CW. Therefore, its magnetization will be negative at H_{v0}, and positive in the W side, being $H_{v0} > 0$. The opposite occurs in the upward branch because vortex circulation inverts. This makes the branches of the HL_E to cross each other twice near $\pm H_{v0}$.

As the field is increased to magnetize the disk in the opposite direction, the core of the vortex moves transverse to the field. This movement is from the E toward the W in the downward branch. This movement starts at a critical field, named H_{v1}. This field has to not be symmetrical to H_{v0}. In the present example, $H_{v1} \approx -15$ mT in HL_W and HL_E. Also, the core movement to the edge might have a different magnetic susceptibility than the changes produced during the creation of the vortex. This makes the HL to develop lobes near the magnetic saturation regions. The steepness of the magnetic susceptibility in the region between H_{v0} and H_{v1} indicates how much the vortex moves in that range of fields. Therefore, this field region gives direct information of the regions of the disk where core vortex is stable. The HLs of the example shows that the vortex is relatively stable in the region from where the HLs are extracted, what is at the region of the disk far from the center. The killing of the vortex is usually produced near saturation fields, causing a different change in the magnetic susceptibility slope. The field where this is produced is named H_s. In this case, the field H_s at which this happens is practically the same, 50 mT, in HL_E and HL_W in the downward branch. Therefore, the magnetization in the W side is always higher than in the E side in the downward branch, explaining the "fat" shape of HL_W, whose branches envelopes those of HL_E. By contrast, the magnetization measured at any point in the center of the disk from the N to the S sides will be zero if the core of the vortex is in the center of the disk since their main magnetic component is transverse to the measured direction.

Figures 11 and 12 show the HLs of Fe and Co at different BR positions in the (11) sample orientation, giving a

more detailed description of the magnetization at different locations of the disks. The BRs are ordered in the horizontal line from negative q_x to positive q_x values, which are related to the magnetization at the regions of the disk running from S to N. The first row is the HLs taken at $q_y = 0$, i.e., the HLs located at the center of the disk. The other two rows have increasing q_y values. They are related to regions of the disk, which are increasingly further from the center, either moving towards the E (HLs in blue) or to the W (HLs in red). The distance Δq between BRs along the q_x and q_y axis is $\sqrt{2}(\pi/\alpha)$. Some of the $[h, k]$ values displayed in the N side are not exactly the same as at the S side because the corresponding HLs are too distorted to be shown. They are at BRs where the magnetic contrast invert their sign. The HLs displayed in the third row are taken at q_y values that are further from the center than the allowed q_x values ($h \leq 4$).

At the cobalt layer, the HL in BR $[0, 0]$ has a coercive field, indicating that the core of the vortex avoids the center of the disk. Note that this HL does not resemble that obtained by VSM (see Fig. 1). The magnetic behavior in the N and S sides is not symmetric with respect to the center. The H_0 and H_s fields are higher in the S side, higher than 60 mT, than in the N side, of the order of 40 mT. Actually, the HL at the extreme S side does not seem to reach saturation. There, the coercive field is null, but it is significant in the N side, which is of about 10 mT. This asymmetry between the N and S sides occurs also in the HLs taken at $q_y \neq 0$. The H_0 field is higher in the S side of the E side (HL in blue), decreasing as q_y becomes more negative, varying from higher than 60 mT to lower than 40 mT. H_0 is the highest in the SE side. It decreases approaching the E side, becoming the same as in the W side. However, H_0 is much smaller in the NE side than in the NW, confirming the different magnetization between the N and S sides of the magnets. Note also that the branches of the HLs in the NE side never cross each other, whereas this clearly happens in the SE side. Therefore, the N side of the disk has a lower probability of holding the core of the vortex than in the S side. The region where the vortex is more stable, i.e., where little changes in the magnetization occurs, is at the edges of the disk (large $|q_y|$ values) since it is where the susceptibility between H_{v0} and H_{v1} is flatter and the distance between both fields is increased. It is in the NE and NW sides where the distance between the H_{v0} and H_{v1} fields is the highest, confirming that most of the changes in the vortex in the cobalt layer occurs mainly in the S side. Moreover, the H_s field is practically the same in the W and E side, indicating that the annihilation of the vortex occurs at the S side, which has the highest saturation field.

The HLs of the iron layer shown in Fig. 12 are of less quality than those of cobalt due to the lower scattered intensity. All of them have the downward branch different than the upward branch, they are not symmetric.
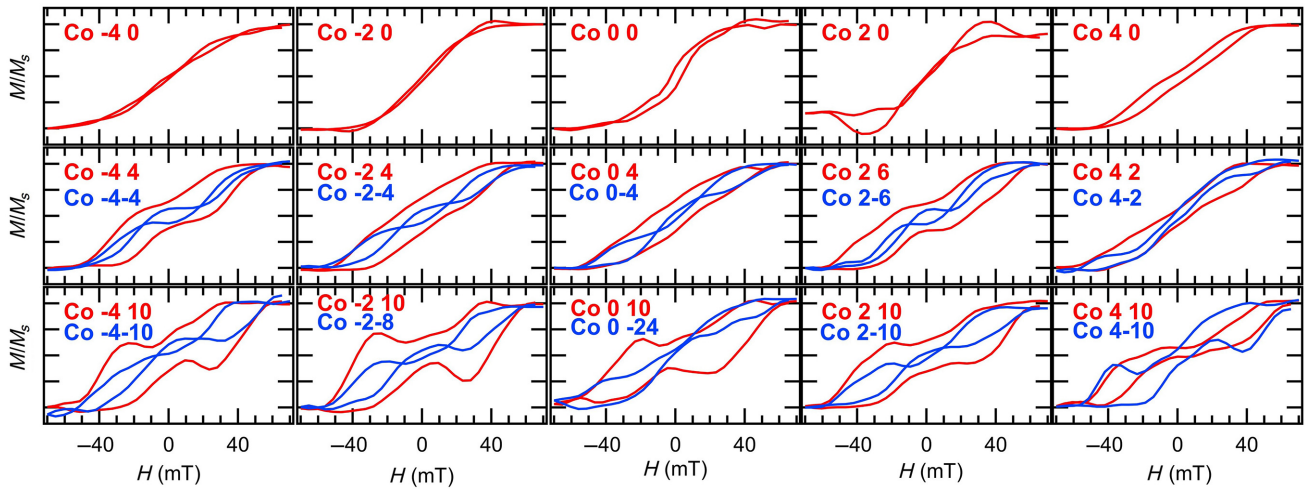
FIG. 11. Hysteresis loops of the cobalt layer in the (11) orientation, at chosen BRs. The way $[h, k]$ numbers locate the BRs is described in the text. N side is at $q_x > 0$, W side is at $q_y > 0$ (red color HLs), and E side is at $q_y < 0$ (blue color HLs).

Both branches cross each other once near $H = 0$. Figure 10 (at the bottom) shows the shape of these HLs more in detail. The start of the downward branch is similar to that of cobalt, which is related to the formation of vortices with the same magnetic circulation sense, CW. The magnetization of the downward branch falls down to lower values at $H \geq$ -10 mT. The reduction of magnetization until saturation from there is done with a slow rate. The value of H_s is of about 55 mT, similar as the saturation fields found in cobalt. The upward branch starts at the same field H_0 as the saturation field. This is a much higher H_0 field than that measured in cobalt. The increase in magnetization is also faster than in the downward branch, stabilizing the vortex at -20 mT. Again, the chirality of this vortex is the same as in cobalt for this orientation of the field, giving rise to a CCW chirality. As in cobalt, the onset field H_0 is higher in

the S side than in the N side. The HL at $[-4, 0]$ has a slope as if magnetic saturation is not complete, something that does not happen at the conjugate BR in $[4, 0]$, with lower saturation fields. Therefore, nucleation starts and dies at the same region than in cobalt.

The annihilation of the vortex is obviously different for the two branches. The change in the magnetization at the field where the vortex in the downward branch is killed is more relevant in the SE side of the disk, indicating that the vortex is preferentially in this region, as in cobalt. Saturation occurs first in the NW side for this branch. For the upward branch, saturation field is higher than in cobalt. Saturation occurs at lower fields in the N side for this loop branch again. In general, saturation is produced first in the NW and at a much higher field in the SE side. The region of the disk where the change in the magnetization in the
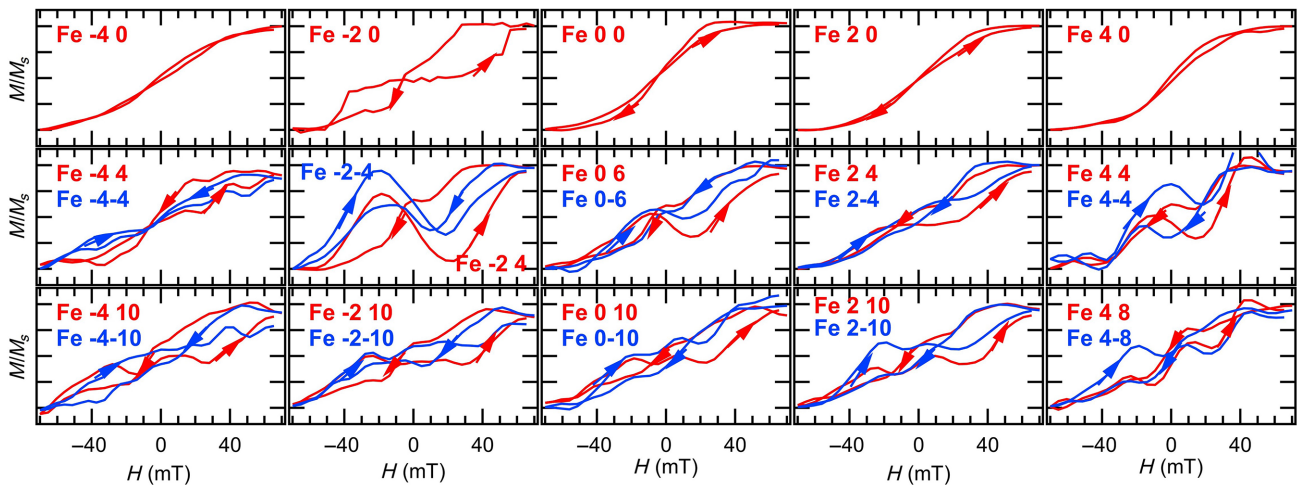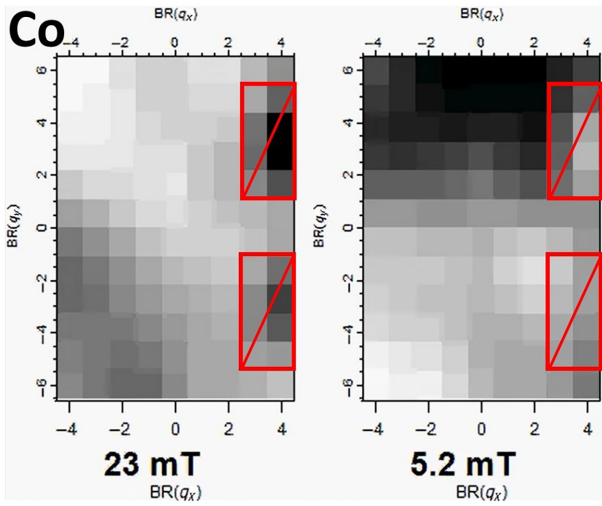

FIG. 12. Hysteresis loops of the iron layer in the (11) orientation, at chosen BRs. The way $[h, k]$ numbers locate the BRs is described in the text. N side is at $q_x > 0$, W side is at $q_y > 0$ (red color HLs), and E side is at $q_y < 0$ (blue color HLs).
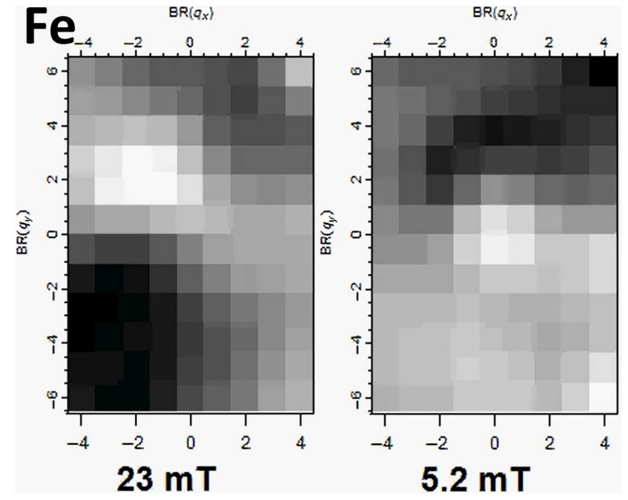
VIDEO 1. The video represents the variation in the normalized magnetic scattering of the cobalt layer at each BR peak (described in the frames by their index $[k, l]$) as a function of the applied field, indicated at the bottom of each frame. The magnetic field is oriented in the horizontal axis of the image. The N side of the magnet is on the right, S on the left, W on top, and E on the bottom. The magnetization is represented by a gray scale: bright white corresponds to the highest magnetization parallel to the N to S orientation, and black is the highest magnetization oriented in the opposite direction. Noise in the images is reduced using a Gaussian filter. The figure shows two frames taken at the downward branch (23 mT) and at the upward branch (5.2 mT). The pixels within the red box correspond to regions where the magnetic contrast change of sign, giving no magnetic signal.

upward branch between H_{v0} and H_{v1} is small, occurs as well in the edges. But the range of fields seems to be larger towards the S side. From these observations, it seems that the core of vortex in the cobalt and iron layers stays in similar regions of the disks. This is unexpected because the poles created by the formation of the vortex in each layer should have repulsive forces.

The videos shown in Videos 1 and 2 give a more visual representation of the changes in the magnetism of the disk described before. The intensity at each pixel of each frame is the magnetic contrast collected at each Bragg reflection at a given applied field normalized to the total magnetic dichroism obtained when the magnets are magnetically saturated. Since the Bragg peaks are due to the interference of light reflected from the same region of the magnets, each frame of the video represents the magnetic configuration of the related layer, averaged over all the illuminated magnets, at the corresponding applied magnetic field. The videos show that demagnetization starts at the SE side, that the movement of the core occurs at the center of the disks and that the saturation is ended at the S side.

Figures 13 and 14 shows the Fe and Co HLs in the (10) orientation for comparison. In this case, there is not a clear asymmetry in the magnetic vortex circulation. The

VIDEO 2. The video represents the same kind of variations in intensity described in video 1 but for the iron layer. The indications given for video 1 are applicable to video 2. The figure shows two frames taken at the downward branch (23 mT) and at the upward branch (5.2 mT).

distance Δq between BRs along the q_x and q_y axis is $2\pi/\alpha$. The HL of the cobalt layer at BR [0, 0] is very similar to that obtained in the (11) orientation. The onset field H_0 is similar in the N and S sides and smaller than in the (11) orientation. Moreover, the highest H_0 seems to be in the E and W sides, at $[0, \pm 3]$ and $[1, \pm 3]$. There, the HLs have a different shape than at the other edges, indicating that it is in this region where the core of the vortex moves. There is still an asymmetry between the N and S sides, as in the (11) orientation. At the S side, the HLs with $q_y \neq 0$ show an imbalance in the chiral symmetry of the magnetic circulation. The magnetic circulation is, in this case, CCW in the downward branch and CW in the upward branch. Surprisingly, such a chiral asymmetry is not observed in the N side, remarking the asymmetry in the magnetic behavior between the two sides of the disk. In this side, the downward branch has an onset H_0 field, which is clearly different than in the downward branch.

In the iron layer, its HL at BR [0, 0] has a coercive field, which is larger than in cobalt. The onset field H_0 is similar in the N and S sides. It is also the highest of the registered for this orientation, but smaller than in the (11) orientation. The asymmetry between the N and S sides is not so clear as in cobalt and there is no chiral asymmetry in the magnetic circulation of the vortex. The distortion of the HLs at the central region is attributed to the mixing of magnetic signals with opposite contrast sign. This similar effect is also observed (and not shown here) in cobalt, but at different BRs.

A. Discussion

Having the same chiral asymmetry in both layers is not the expected behavior since the nucleation of the vortex
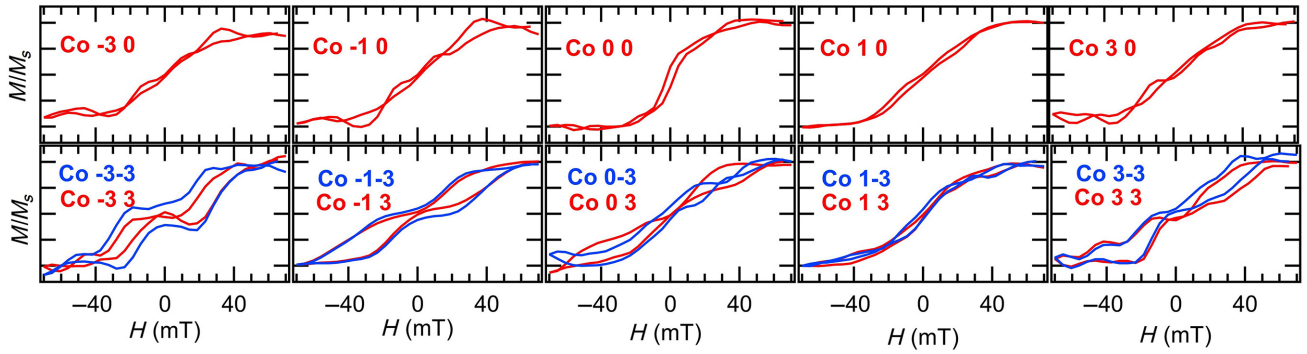
FIG. 13. Hysteresis loops of the cobalt layer in the (10) orientation, at chosen BRs, $[q_x, q_y] = [h, k]$ and in conjugated sites ($[h, \pm k]$). The N side is at $q_x > 0$, the W side is at $q_y > 0$ (red color HLs).

in each layer creates magnetic poles of the same sign. This makes it energetically more favorable for each disk to do the nucleation at opposite sides of the border of the disk, inducing an opposite chiral sense in each layer [5]. This is in fact very critical in this case because the region where the disk begins to demagnetize seems to be the same in both layers and for the two orientations of the saturated magnetization in the disks. Therefore, the origin of the asymmetry has to be related either to a more energy-lowering process that should over compensate the expected polar repulsion between the two layers, or because there is an effective attractive interlayer interaction. The large saturation fields measured in the trilayer magnets, which are similar to noninteracting single-layer disk at distances, are where intermagnet interaction is expected, suggesting this last possibility. This should be induced by the roughness of the interfaces (Néel peel orange effect [41]) and/or the observed thickness gradient.

The observed type of chiral asymmetry, with changes of sign depending on the initial magnetization direction, is induced in submicron magnets by making their shape noncentrosymmetric: triangles, truncated disks, asymmetric rings, "pac-man"-shaped disks or asymmetrical magnetic moment distribution [2,15,42–46]. Chiral asymmetry

occurs in these systems when the applied field is at an angle with respect to the mirror symmetry axis of the system.

To explain the origin of the chiral asymmetry in the studied system, we propose the following model based on the existence of a noncentrosymmetry in the magnets of the array. In the (10) field orientation, the cobalt layer contains a magnetic asymmetry. Such an asymmetry might be related to the anisotropy energy which could be asymmetrically distributed across the area of the disk. This could happen if its shape is not fully symmetric. In this case, the S side has possibly a higher anisotropy than the N side, what is required to preserve mirror symmetry between the W and E sides, since chiral asymmetry is not fully manifested in this orientation [44]. In the (11) orientation, the oblique angle direction of the applied field breaks such a mirror symmetry causing the observed chiral asymmetry. Then, when the direction of the field is positive, the moments in the N side have a weaker anisotropy and align their moments with the applied field at lower fields than in the S side. This creates an in-plane component of the magnetization perpendicular to the direction of the field at that particular region, setting the sense of rotation of the magnetization in the vortex. When the direction of the field is the opposite, the orientation of this in-plane
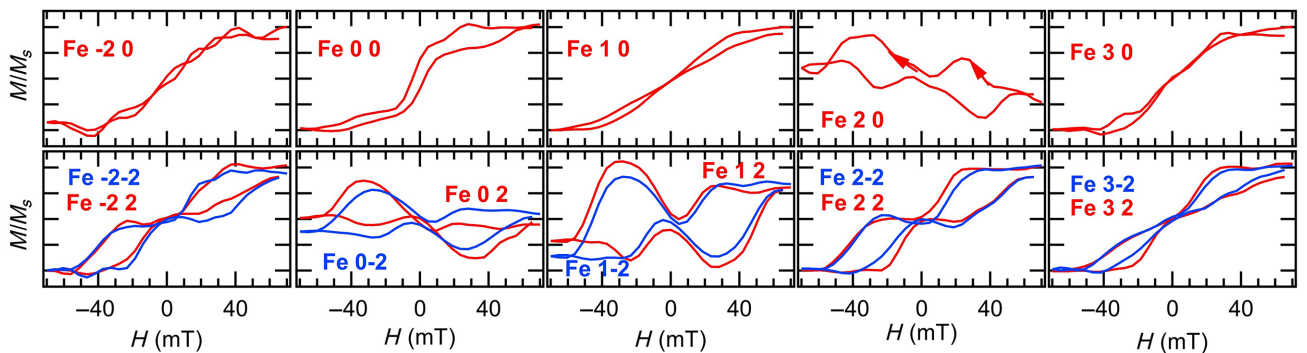

FIG. 14. Hysteresis loops of the iron layer in the (10) orientation, at chosen BR, $[q_x, q_y] = [h, k]$ and in conjugated sites ($[h, \pm k]$). The N side is at $q_x > 0$, the W side is at $q_y > 0$ (red color HLs).
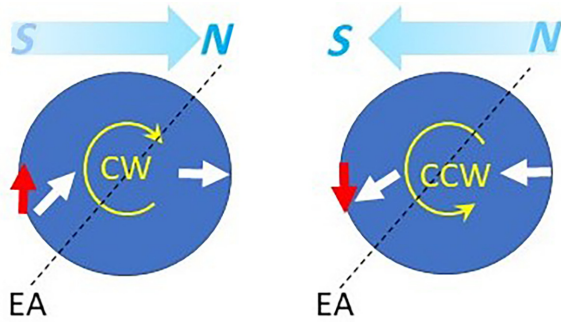
FIG. 15. Model proposed to explain the chiral asymmetry in the array of disks. The black dashed line diagonally crossing the disks is the EA. The magnetic field in the left (right) disk points toward the N (S) and it is gradually reduced from saturation to zero. In the two disks, their S side has a higher magnetic anisotropy than in the N side. The white arrows indicate the mean magnetization orientation in these sides of the disks at a lower than saturation field. The SE side requires a higher magnetic field to saturate. The red arrow is the projection of the magnetization of the SE side in the direction perpendicular to the field, changing the sign depending on the direction of the applied field. It induces the direction of magnetic circulation of the vortex in the disks.

perpendicular component changes its direction as well, changing the sense of the magnetic circulation of the vortex to the opposite one. The model is depicted in Fig. 15. This process seems to be very solid in the cobalt layer since the branches of its HLs are symmetric at any point in the disk. It is also the layer that register an asymmetry between N and S sides in the (10) orientation as well.

Figure 16 shows the fast Fourier transform (FFT) of the image obtained by SEM of the sample, which includes more than 10^3 disks. A visual inspection shows that the intensity of the peaks deviates from the expected symmetric square shape resulting from the FFT of a diamond shape. A detailed analysis of the intensity of the BR peaks in this figure shows that the ideally diamond-shape disks are actually rhomboids. Their shape asymmetry arises because the distance between opposite sides of the diamondlike shape of the disks are not exactly the same. This makes the shape of the disks noncentrosymmetric, i.e., there is not perfect mirror symmetry across any of the symmetry axis oriented along the (10), (01), (11), or (-1-1) directions. This deviation from centrosymmetry in the shape of the magnets is much smaller than the noncentrosymmetry induced in magnets by purpose to fix their vortex chirality. This might indicate that a precise control of the ILL technique can be used to modulate the chiral properties of magnet arrays by inducing asymmetries in their shape.

Since the HL measurement is done in a single cycle, it is not possible to assert that the different magnetization paths taken in each of the branches of the HL in Fe in the (11) orientation, and the observed in some HLs in
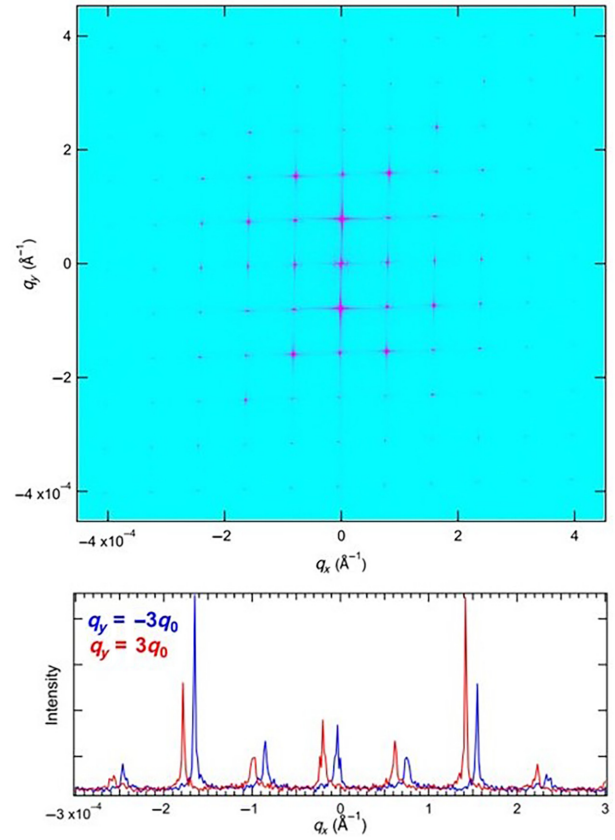

FIG. 16. Fourier transform of a SEM image of the array including more than 10^3 disks. On the bottom, the intensity of q_x scans across the previous image in two opposite values of q_y to evidence the deviation from perfect mirror symmetry with respect to the (10) and (01) axes. Scans have their q_x zero shifted for better comparison. $q_0 = 2\pi/\alpha$ where α is the lattice constant of the array.

the (10) orientation, is a systematic and repetitive process. The HL measured by VSM, which covers a much larger area than the measured by XRMS, did not show any asymmetry between the branches. Therefore, these asymmetries are possibly due to a certain stochasticity in the magnetic inversion process of the disks, which have to be collective by the nature of the measurement. This effect is likely produced by thermal fluctuations due to the small size of the disks and the relatively large x-ray exposure time.

VI. CONCLUSIONS

In conclusion, we observe a one-to-one correlation between the in-plane moment vector transfer of the scattered light from an array of submicron magnets and the spatial location in the magnets from where the light comes, converting the magnetic contrast of the diffraction pattern of the array in an image of the average magnetic configuration of the magnets at each applied field. The conditions for this to happen are related to the morphology of the

magnets and the configuration of the experiment. The surface of the magnets must have a certain curvature. In the present experiment, this is obtained using magnetron sputtering deposition at normal incidence in patterned holes, which is one of the most used methods to produce the kind of studied magnet arrays. The grazing incidence angles employed are relatively large to allow the collection of scattered light at a wider range of in-plane moment transfer. At such large angles, the diffuse scattering due to the roughness and imperfections at the layer interfaces should be relevant when joined to the resonant energies employed, allowing a better isolation of the targeted layers even if they are buried under 20-nm-thick layers. This kind of magnetic microscope effect explains why XRMS is specially sensitive to the chiral asymmetry of the magnetization circulation of the vortex formed in the magnets. Thanks to this effect, it is possible to identify the presence of a noncentrosymmetry in the magnetization of the sample that explains the apparition of the chiral asymmetry at the oblique angle orientation of the field with respect to the EA axis of the array. The physical origin of such a magnetic noncentrosymmetry was attributed to deviations from centrosymmetry in the shape of the magnets, giving an indication of the sensitivity of the studied system to such deviations. Moreover, the same chirality is found in the two layers indicating that their interlayer magnetic interaction is attractive. The presented experiment shows that XRMS can give a collective vision of the stability and symmetry-breaking process in this kind of system, which is hardly obtained by other microscopic techniques. There is plenty of room to increase the quality of the data and to increase the information extracted from the scattered light. For instance, the transverse component of the magnetization can also be obtained by using linearly polarized light, making it possible to give a complete characterization of the in-plane magnetization of the magnets at any applied field. This technique is particularly well suited for the study of magnets with magnetic buried layers whose properties are less known than those of single-layer magnets, but that could have a wider range of application and functionalities.

[1] K. Y. Guslienko, V. Novosad, Y. Otani, H. Shima, and K. Fukamichi, Field evolution of magnetic vortex state in ferromagnetic disks, Appl. Phys. Lett. **78,** 3848 (2001).

[2] M. Schneider, H. Hoffmann, and J. Zweck, Magnetic switching of single vortex permalloy elements, Appl. Phys. Lett. **79,** 3113 (2001).

[3] M. Grimsditch, P. Vavassori, V. Novosad, V. Metlushko, H. Shima, Y. Otani, and K. Fukamichi, Vortex chirality in an array of ferromagnetic dots, Phys. Rev. B **65,** 172419 (2002).

[4] K. S. Buchanan, K. Y. Guslienko, A. Doran, A. Scholl, S. D. Bader, and V. Novosad, Magnetic remanent states and magnetization reversal in patterned trilayer nanodots, Phys. Rev. B **72,** 134415 (2005).

[5] K. Y. Guslienko and M. S. Division, Magnetic vortex state stability, reversal and dynamics in restricted geometries, J. Nanosci. Nanotechnol. **8,** 2745 (2008).

[6] J.-G. Zhu, Y. Zheng, and G. A. Prinz, Ultrahigh density vertical magnetoresistive random access memory, J. Appl. Phys. **87,** 6668 (2000).

[7] B. Pigeau, G. de Loubens, O. Klein, A. Riegler, F. Lochner, G. Schmidt, L. W. Molenkamp, V. S. Tiberkevich, and A. N. Slavin, A frequency-controlled magnetic vortex memory, Appl. Phys. Lett. **96,** 132506 (2010).

[8] K. Y. Guslienko, K. S. Buchanan, S. D. Bader, and V. Novosad, Dynamics of coupled vortices in layered magnetic nanodots, Appl. Phys. Lett. **86,** 223112 (2005).

[9] S. Wintz, V. Tiberkevich, M. Weigand, J. Raabe, J. Lindner, A. Erbe, A. Slavin, and J. Fassbender, Magnetic vortex cores as tunable spin-wave emitters, Nat. Nanotechnol. **11,** 948 (2016).

[10] D. Suess, A. Bachleitner-Hofmann, A. Satz, H. Weitensfelder, C. Vogler, F. Bruckner, C. Abert, K. Prügl, J. Zimmer, C. Huber, S. Luber, W. Raberg, T. Schrefl, and H. Brückl, Topologically protected vortex structures for low-noise magnetic sensors with high linear range, Nat. Electron. **1,** 362 (2018).

[11] M. Endo, M. Al-Mahdawi, M. Oogane, and Y. Ando, Control of sensitivity in vortex-type magnetic tunnel junction magnetometer sensors by the pinned layer geometry, J. Phys. D: Appl. Phys. **55,** 195001 (2022).

[12] T. Wurft, W. Raberg, K. Prügl, A. Satz, G. Reiss, and H. Brückl, Evolution of magnetic vortex formation in micronsized disks, Appl. Phys. Lett. **115,** 132407 (2019).

[13] D.-H. Kim, E. A. Rozhkova, I. V. Ulasov, S. D. Bader, T. Rajh, M. S. Lesniak, and V. Novosad, Biofunctionalized magnetic-vortex microdiscs for targeted cancer-cell destruction, Nat. Mater. **9,** 165 (2010).

[14] L. Peixoto, R. Magalhães, D. Navas, S. Moraes, C. Redondo, R. Morales, J. P. Araújo, and C. T. Sousa, Magnetic nanostructures for emerging biomedical applications, Appl. Phys. Rev. **7,** 011310 (2020).

[15] L. Huang, M. A. Schofield, and Y. Zhu, Control of double-vortex domain configurations in a shape-engineered trilayer nanomagnet system, Adv. Mater. **22,** 492 (2010).

[16] P. Vavassori, V. Bonanni, A. Busato, D. Bisero, G. Gubbiotti, A. O. Adeyeye, S. Goolaup, N. Singh, C. Spezzani, and M. Sacchi, Magnetostatic and exchange coupling in the magnetization reversal of trilayer nanodots, J. Phys. D: Appl. Phys. **41,** 134014 (2008).

[17] A. Parente, H. Navarro, N. M. Vargas, P. Lapa, A. C. Basaran, E. M. González, C. Redondo, R. Morales, A. Munoz Noval, I. K. Schuller, and J. L. Vicent, Unusual

magnetic hysteresis and transition between vortex and double pole states arising from interlayer coupling in diamond-shaped nanostructures, ACS Appl. Mater. Interfaces **14,** 54961 (2022).

[18] T. Okuno, K. Shigeto, T. Ono, K. Mibu, and T. Shinjo, MFM study of magnetic vortex cores in circular permalloy dots: Behavior in external field, J. Magn. Magn. Mater. **240,** 1 (2002),4th International Symposium on Metallic Multilayers.

[19] M. Coïsson, G. Barrera, F. Celegato, A. Manzin, F. Vinai, and P. Tiberto, Magnetic vortex chirality determination via local hysteresis loops measurements with magnetic force microscopy, Sci. Rep. **6,** 29904 (2016).

[20] O. Kazakova, R. Puttock, C. Barton, H. Corte-León, M. Jaafar, V. Neu, and A. Asenjo, Frontiers of magnetic force microscopy, J. Appl. Phys. **125,** 060901 (2019).

[21] C. Holl, M. Knol, M. Pratzer, J. Chico, I. L. Fernandes, S. Lounis, and M. Morgenstern, Probing the pinning strength of magnetic vortex cores with sub-nanometer resolution, Nat. Commun. **11,** 2833 (2020).

[22] J. Wu, D. Carlton, E. Oelker, J. S. Park, E. Jin, E. Arenholz, A. Scholl, C. Hwang, J. Bokor, and Z. Q. Qiu, Switching a magnetic vortex by interlayer coupling in epitaxially grown Co/Cu/Py/Cu(001) trilayer disks, J. Phys.: Condens. Matter **22,** 342001 (2010).

[23] M. Schneider, H. Hoffmann, and J. Zweck, Lorentz microscopy of circular ferromagnetic permalloy nanodisks, Appl. Phys. Lett. **77,** 2909 (2000).

[24] O. Geoffroy, D. Givord, Y. Otani, B. Pannetier, A. Santos, M. Schlenker, and Y. Souche, TMOKE hysteresis loops in Bragg diffraction from 2D patterns, J. Magn. Magn. Mater. **121,** 516 (1993),Proceedings of the International Symposium on Magnetic Ultrathin Films, Multilayers and Surfaces.

[25] J. L. Costa-Krämer, C. Guerrero, S. Melle, P. García-Mochales, and F. Briones, Pure magneto-optic diffraction by a periodic domain structure, Nanotechnology **14,** 239 (2003).

[26] M. Grimsditch and P. Vavassori, The diffracted magneto-optic Kerr effect: What does it tell you?, J. Phys.: Condens. Matter **16,** R275 (2004).

[27] A. Westphalen, M.-S. Lee, A. Remhof, and H. Zabel, Invited article: Vector and Bragg magneto-optical Kerr effect for the analysis of nanostructured magnetic arrays, Rev. Sci. Instrum. **78,** 121301 (2007).

[28] M.-S. Lee, A. Westphalen, A. Remhof, A. Schumann, and H. Zabel, Extended longitudinal vector and Bragg magneto-optic Kerr effect for the determination of the chirality distribution in magnetic vortices, J. Appl. Phys. **103,** 093913 (2008).

[29] G. van der Laan, Soft x-ray resonant magnetic scattering of magnetic nanostructures, C. R. Phys. **9,** 570 (2008),Synchrotron X-rays and condensed matter.

[30] Y. Choi, D. R. Lee, J. W. Freeland, G. Srajer, and V. Metlushko, Layer-resolved study of magnetic interaction effects in heterostructure dot arrays, Appl. Phys. Lett. **88,** 112502 (2006).

[31] V. Rose, X. M. Cheng, D. J. Keavney, J. W. Freeland, K. S. Buchanan, B. Ilic, and V. Metlushko, The breakdown of

the fingerprinting of vortices by hysteresis loops in circular multilayer ring arrays, Appl. Phys. Lett. **91,** 132501 (2007).

[32] D. R. Lee, J. W. Freeland, Y. Choi, G. Srajer, V. Metlushko, and B. Ilic, X-ray resonant magnetic scattering study of magnetization reversals in a nanoscale spin-valve array, Phys. Rev. B **76,** 144425 (2007).

[33] F. Tejo, D. Toneto, S. Oyarzún, J. Hermosilla, C. S. Danna, J. L. Palma, R. B. da Silva, L. S. Dorneles, and J. C. Denardin, Stabilization of magnetic skyrmions on arrays of self-assembled hexagonal nanodomes for magnetic recording applications, ACS Appl. Mater. Interfaces **12,** 53454 (2020).

[34] J. Díaz, P. Gargiani, C. Quirós, C. Redondo, R. Morales, L. M. Álvarez Prado, J. I. Martín, A. Scholl, S. Ferrer, M. Vélez, and S. M. Valvidares, Chiral asymmetry detected in a 2D array of permalloy square nanomagnets using circularly polarized x-ray resonant magnetic scattering, Nanotechnology **31,** 025702 (2019).

[35] B. Mora, A. Perez-Valle, C. Redondo, M. D. Boyano, and R. Morales, Cost-effective design of high-magnetic moment nanostructures for biotechnological applications, ACS Appl. Mater. Interfaces **10,** 8165 (2018).

[36] V. Novosad, K. Y. Guslienko, H. Shima, Y. Otani, S. G. Kim, K. Fukamichi, N. Kikuchi, O. Kitakami, and Y. Shimada, Effect of interdot magnetostatic interaction on magnetization reversal in circular dot arrays, Phys. Rev. B **65,** 060402(R) (2002).

[37] A. Barla, J. Nicolás, D. Cocco, S. M. Valvidares, J. Herrero-Martín, P. Gargiani, J. Moldes, C. Ruget, E. Pellegrin, and S. Ferrer, Design and performance of boreas, the beamline for resonant x-ray absorption and scattering experiments at the alba synchrotron light source, J. Synchrotron. Radiat. **23,** 1507 (2016).

[38] M. Elzo, E. Jal, O. Bunau, S. Grenier, Y. Joly, A. Ramos, H. Tolentino, J. Tonnerre, and N. Jaouen, X-ray resonant magnetic reflectivity of stratified magnetic structures: Eigenwave formalism and application to a W/Fe/W trilayer, J. Magn. Magn. Mater. **324,** 105 (2012).

[39] Z. Lazić, V. Chamritski, D. Pooke, S. M. Valvidares, E. Pellegrin, S. Ferrer, X. Granados, and X. Obradors, Integrating UHV (ultra high vacuum) and HTS (high temperature superconducting) magnets for x-ray synchrotron based experiments, J. Phys.: Conf. Ser. **425,** 102003 (2013).

[40] D. R. Lee, S. K. Sinha, D. Haskel, Y. Choi, J. C. Lang, S. A. Stepanov, and G. Srajer, X-ray resonant magnetic scattering from structurally and magnetically rough interfaces in multilayered systems. I. Specular reflectivity, Phys. Rev. B **68,** 224409 (2003).

[41] B. D. Schrag, A. Anguelouch, S. Ingvarsson, G. Xiao, Y. Lu, P. L. Trouilloud, A. Gupta, R. A. Wanner, W. J. Gallagher, P. M. Rice, and S. S. P. Parkin, Néel "orange-peel" coupling in magnetic tunneling junction devices, Appl. Phys. Lett. **77,** 2373 (2000).

[42] R. K. Dumas, D. A. Gilbert, N. Eibagi, and K. Liu, Chirality control via double vortices in asymmetric co dots, Phys. Rev. B **83,** 060415(R) (2011).

[43] M. Jaafar, R. Yanes, D. Perez de Lara, O. Chubykalo-Fesenko, A. Asenjo, E. M. Gonzalez, J. V. Anguita, M.

Vazquez, and J. L. Vicent, Control of the chirality and polarity of magnetic vortices in triangular nanodots, Phys. Rev. B **81**, 054439 (2010).

[44] S. Agramunt-Puig, N. Del-Valle, C. Navau, and A. Sanchez, Controlling vortex chirality and polarity by geometry in magnetic nanodots, Appl. Phys. Lett. **104**, 012407 (2014).

[45] V. Cambel and G. Karapetrov, Control of vortex chirality and polarity in magnetic nanodots with broken rotational symmetry, Phys. Rev. B **84**, 014424 (2011).

[46] Z. Zhong, H. Zhang, X. Tang, Y. Jing, L. Jia, and S. Liu, Vortex chirality control in magnetic submicron dots with asymmetrical magnetic properties in lateral direction, J. Magn. Magn. Mater. **321**, 2345 (2009).